Frontiers of Information Technology & Electronic Engineering
www.jzus.zju.edu.cn; engineering.cae.cn; www.springerlink.com
ISSN 2095-9184 (print); ISSN 2095-9230 (online)
E-mail: jzus@zju.edu.cn

Empirical study on directional millimeter-wave propagation in vehicle-to-infrastructure communications between road and roadside*

Xichen LIU, Lin YANG‡, Daizhong YU

National Key Laboratory of Science and Technology on Communication, University of Electronic Science and Technology of China, Chengdu 611731, China

E-mail: 362475709@qq.com; eelyang@uestc.edu.cn; 15908107465@163.com

Received Sept. 8, 2020; Revision accepted Feb. 18, 2021; Crosschecked Mar. 5, 2021

Abstract: With the increased demand for unmanned driving technology and big-data transmission between vehicles, millimeter-wave (mmWave) technology, due to its characteristics of large bandwidth and low latency, is considered to be the key technology in future vehicular communication systems. Different from traditional cellular communication, the vehicular communication environment has the characteristics of long distance and high moving speed. However, the existing communication channel tests mostly select low-speed and small-range communication scenarios for testing. The test results are insufficient to provide good data support for the existing vehicular communication research; therefore, in this paper, we carry out a large number of channel measurements in mmWave vehicle-to-infrastructure (V2I) long-distance communication scenarios in the 41 GHz band. We study the received signal strength (RSS) in detail and find that the vibration features of RSS can be best modeled by the modified two-path model considering road roughness. Based on the obtained RSS, a novel close-in (CI) model considering the effect of the transmitter (TX) and receiver (RX) antenna heights (CI-TRH model) is developed. As for the channel characteristics, the distribution of the root-mean-square (RMS) delay spread is analyzed. We also extend the two-section exponential power delay profile (PDP) model to a more general form so that the distance-dependent features of the mmWave channel can be better modeled. Furthermore, the variation in both RMS delay spread and PDP shape parameters with TX-RX distance is analyzed. Analysis results show that TX and RX antenna heights have an effect on large-scale fading. Our modified two-path model, CI-TRH model, and two-section exponential PDP model are proved to be effective.

Key words: Millimeter-wave; Two-path model; Root-mean-square delay spread; Power delay profile; CI-TRH path-loss model

https://doi.org/10.1631/FITEE.2000464 **CLC number:** TN928

1 Introduction

With the continuous increase of car ownership in recent years, issues such as traffic safety and travel efficiency are becoming increasingly prominent, resulting in an increasing demand for high-speed mobile communications. To solve these problems, high-rate communication systems for vehicles are urgently needed. Traditional communication systems use mostly the frequency band below 6 GHz

‡ Corresponding author

* Project supported by the National Key Research and Development Program of China (No. 2020YFB1805001), the National Natural Science Foundation of China (Nos. 91938202 and 61801102), the Defense Industrial Technology Development Program, China (No. JCKY2016204A603), and the 5G Millimeter Wave High-Speed Channel Simulator, China (No. 2021YFG0342)

ORCID: Xichen LIU, https://orcid.org/0000-0002-9776-313X; Lin YANG, https://orcid.org/0000-0001-7369-796X

for communication, but with the arrival of the fifth-generation mobile communication (5G) system era, the frequency resources of the low-frequency band have been divided up. The high-frequency band, especially the millimeter-wave (mmWave) band, is getting increasing attention due to its ability to increase the communication bandwidth and the additional resources on frequency. In addition to the above advantages, mmWave communication systems equipped with large-scale phased array antennas can be miniaturized due to the small wavelength of the mmWave (Yang et al., 2019).

Compared with today's cellular frequencies, the wavelengths of mmWave are much smaller than those of sub-6 GHz systems, which means that mmWave undergoes greater free space attenuation in the first meter of propagation due to the Friis free space equation. At some frequency bands, such as 60, 180, 330, or 380 GHz, molecular resonances can make signals attenuate much more rapidly (Rappaport et al., 2015). Besides, the designs of mmWave communication systems are highly dependent on the wireless channel characteristics under various environments; therefore, it is necessary for researchers to study mmWave channels in different scenarios.

The mmWave propagation characteristics in indoor short-distance transmission scenarios, such as the office at 28 GHz (Lei et al., 2016), the conference room and lobby at 39 GHz (Zhang et al., 2019), and the non-line-of-sight (NLoS) situation in a corridor at 41 GHz (Yue et al., 2019a), have been studied widely. Moreover, railway communication scenarios are considered in mmWave applications, including high-speed railway (He et al., 2018) and high-speed train (Yue et al., 2019b) communication systems, train-to-infrastructure scenarios (Meinel and Plattner, 1983), measurements of the four types of angular spreads (Guan et al., 2018), and the impact of vibration between wagons (Soliman et al., 2018).

The mmWave vehicular communication scenarios can be classified roughly into three main categories, in-car, vehicle-to-vehicle (V2V), and vehicle-to-infrastructure (V2I) scenarios. In in-car communication scenarios, the vibration of the car has a significant impact on the mmWave channel; research in this area is focused on the estimation of Doppler spread (Blumenstein et al., 2016; Rahman et al., 2019), the investigation of the time-varying intravehicle channel under various traffic conditions (Prokes et al., 2016), and the dependency of the Rician K-factor on road quality and velocity (Blumenstein et al., 2017). For V2V scenarios, the various channel characteristics including large-scale fading (such as path loss) and small-scale fading (such as the distribution of the path envelope) have been analyzed (Prokes et al., 2018). For example, emphasis has been placed on different channel characteristics when the transmitter (TX) and the receiver (RX) are driving in the same (Boban et al., 2019) or the reverse (Bernadó et al., 2015) directions. The impact of vehicular blockage has been investigated by Sánchez et al. (2017). There is a special scenario, namely, the impact of overtaking of vehicles of different speeds, types (Zöchmann et al., 2018), and positions (Zöchmann et al., 2019).

For V2I communications, channel characteristics are studied through measurements, ray-tracing simulations, and performance analysis. For instance, measurements have been conducted by Blumenstein et al. (2018) to investigate the power delay profile (PDP) characteristics in an urban-highway environment with 59.6 GHz center frequency and 8 GHz bandwidth. He et al. (2019) have studied the 28 GHz V2I channel characteristics through calibrated ray-tracing simulations. Moreover, the average down stream packet broadcast performance under V2I channel conditions has been reported by Mecklenbrauker et al. (2011). Some other interesting research works include the measurement of V2I Doppler shift at 28 GHz (Park et al., 2018), the 60 GHz multiple-input multiple-output (MIMO) channel sparsity in the delay-Doppler domain (Groll et al., 2019), and both the V2I measurement and simulation of channels under different environments (Yan et al., 2020).

However, recent studies of vehicular communication scenarios are focused mainly on the short-distance propagation characteristics at mmWave bands. The long-distance propagation characteristics at mmWave frequencies are neglected by most studies. In fact, long-distance transmission can be an important application scenario in future V2I communications. For example, in long straight highways and rural avenues (such as the Tianfu Avenue, Chengdu, China), the vehicle speed can reach 100 km/h, and long-distance (>1 km) communication links (Yue et al., 2019b) are crucial to guarantee the link reliability and high quality of service. In

addition, the major concerns of most recent studies are the impacts of other vehicles such as blockage in the overtaking case, but the impacts of some other important factors, such as reflections from the floor, roughness of the ground, influence of the heights of TX and RX, and influence of the distance variation, on the channel parameters have been poorly investigated.

In this work, we conduct extensive measurements of the V2I communication channel characteristics in the 41 GHz band for long-distance (1900 m) transmission. A two-path model considering road roughness is established to model our measurement scenario. Our channel-testing method involves time-domain measurement, which is based on the autocorrelation of the Gray sequence to extract the small-scale fading factor of the channel. At the same time, according to the received signal strength indication (RSSI) of the obtained signal, the large-scale fading parameters of the channel are extracted. A novel CI-TRH model considering the effect of the heights of TX and RX antennas is developed. Moreover, we study the root-mean-square (RMS) delay spread, PDP, and other main parameters. A two-section exponential PDP model is extended to a more general form so that the distance-dependent features of the mmWave channel can be better modeled.

2 Measurement system

2.1 Measurement design

The key parameters for our measurement system are listed in Table 1. We put emphasis on studying the mmWave channel at the Q-band (41 GHz). To obtain a delay resolution of 1 ns with 625 MHz bandwidth, a roll-off factor of 0.25 is used so that the symbol rate is 500 Msym/s. In the RX, we adopt the double symbol-sampling rate.

According to the odd and even sampling rates, the odd and even sampling points can recover the channel at their own time. As a result, a delay resolution of 1 ns is formed. High-gain (24 dBi, decibels relative to isotropic) directive horn antennas with a 10° half-power beamwidth (HPBW) are used. Taking advantages of the high antenna gain, the mmWave detector is able to detect mmWave signals after the high signal attenuation caused by long-distance propagation. The channel transceiver is shown in Fig. 1; it can operate as a TX or an RX. The digital baseband consists of an analog-to-digital converter (ADC) AD6688, a digital-to-analog converter (DAC) AD9163, two XC7VX690T field programmable gate arrays (FPGAs), and a ZYNQ-7045 chip. At the RX radio frequency (RF) front end, an AD8362 chip is used behind the down converter to record RSSI values.

Table 1 Parameters of the mmWave channel sounder in the 41 GHz band

Parameter	Value
Carrier frequency (GHz)	41
Bandwidth (MHz)	625
Symbol rate (Msym/s)	500
TX and RX antenna heights (m)	2
Antenna maximum gain (dBi)	24
Antenna HPBW (°)	10
TX RF output power (dBm)	17
Intermediate frequency of TX (GHz)	0.5–1.5
Intermediate frequency of RX (GHz)	2.5–3.5
Receiver sensitivity (dBm)	−75
TX and RX polarization	Vertical
ADC sampling rate (GHz)	2
RSSI sample rate (kHz)	1
Golay sequence length	256
Multipath time resolution (ns)	1
Transmission technology	Single carrier
Modulation scheme	QPSK
LDPC rate	0.5
Roll-off factor or RC filter	0.25

ADC: analog-to-digital converter; dBi: decibels relative to isotropic; dBm: decibel relative to one milliwatt; HPBW: half-power beamwidth; mmWave: millimeter-wave; RF: radio frequency; RSSI: received signal strength indicator; RX: receiver; TX: transmitter; LDPC: low density parity check code

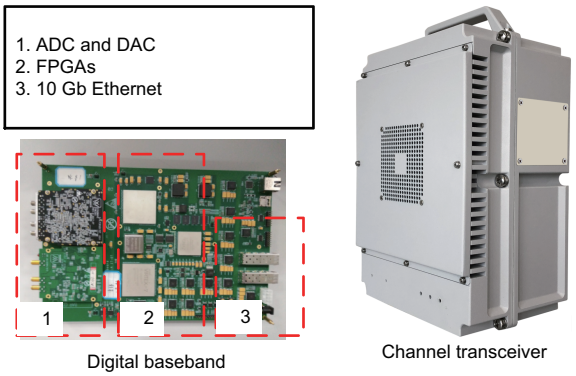

Fig. 1 41 GHz mmWave communication channel transceiver and its hardware prototype

ADC: analog-to-digital converter; DAC: digital-to-analog converter; mmWave: millimeter-wave

With a 65 dB measurement range, the AD8362 chip is a true RMS-responding power detector

(Analog Devices, 2013). It is suitable for all kinds of high-frequency communication systems and instruments that need to provide an accurate response to the signal power; thus, it has been adopted in recent studies to record the received signal strength (RSS) (Yu et al., 2019). Both the digital baseband and the RF front end are sealed in a cabinet that is connected with a 10 Gb optical interface. As a result, the mmWave transceiver is able to communicate with upper layer services through the 10 Gb Ethernet. The polarization mode of these antennas is vertical polarization in both TX and RX, so our results contain only the V2V polarized components. The measured three-dimensional (3D) antenna beam patterns, including the vertical and horizontal plane patterns, are shown in Fig. 2.

2.2 Frame structure

We adopt a time-domain channel measurement method based on Golay complementary sequence pairs to complete the measurement of channel impulse responses (CIRs) in V2I scenarios. In addition to excellent correlation properties, such a sequence can offer an efficient, parallel hardware implementation of the corresponding correlator. The matched filter of the Golay sequence has a fast implementation algorithm, which facilitates the consumption of less hardware resource and ensures the work at high frequency (Popović, 1999).

We define a pair of sequences of length N:

$$G_a = (G_{a_0}, G_{a_1}, \cdots, G_{a_{N-1}}), \tag{1}$$

$$G_b = (G_{b_0}, G_{b_1}, \cdots, G_{b_{N-1}}). \tag{2}$$

Complementary Golay sequences have the important property that the sum of the auto-correlation coefficients of the two complementary sequences will have a unique peak and zero sidelobe, which can be expressed as follows:

$$R_a(i) + R_b(i) = \begin{cases} 2N, & i = 0, \\ 0, & i \neq 0, \end{cases} \tag{3}$$

where $R_a(i)$ and $R_b(i)$ are the auto-correlation functions of sequences G_a and G_b, respectively:

$$R_a(i) = \begin{cases} \sum_{k=0}^{k=N-i-1} G_{a_k} G_{a_{k+i}}, & 0 \le i \le N-1, \\ 0, & \text{else}, \end{cases} \tag{4}$$

$$R_b(i) = \begin{cases} \sum_{k=0}^{k=N-i-1} G_{b_k} G_{b_{k+i}}, & 0 \le i \le N-1, \\ 0, & \text{else}. \end{cases} \tag{5}$$

At the TX side, each transmitted frame consists of some basic elements, such as the guard interval (GI), the short training field (STF), and the channel estimation field (CEF). All of these basic elements are composed of complementary Golay sequences of length 128, denoted as $G_{a_{128}}$ and $G_{b_{128}}$ (IEEE, 2012).

The presentation of a CEF is as follows:

$$(G_{b_{128}}, G_{a_{128}}, -G_{b_{128}}, G_{a_{128}}), \tag{6}$$

which is a Golay sequence of length 512. The first half of the CEF in fact is a 256-unit-long Golay sequence $G_{a_{256}}$, and the other part becomes $G_{b_{256}}$. By applying the property formulated in Eq. (3), a perfect length-256 Dirac-delta function can be recovered. If $G_{a_{256}}$ and $G_{b_{256}}$ sequences pass through the wireless channel and correlate with the local $G_{a_{256}}$ and $G_{b_{256}}$ at the RX, CIR of the wireless channel

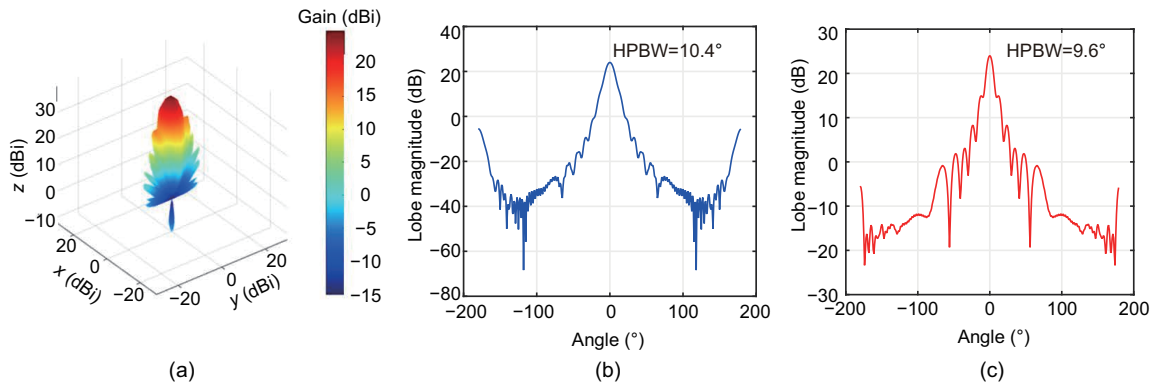

Fig. 2 Three-dimensional beam pattern (a), horizontal plane pattern (b), and vertical plane pattern (c) of the directional antenna used in the measurements (HPBW: half-power beamwidth)

can be recovered with the desirable accuracy (Yue et al., 2019a). Interested readers can refer to Yue et al. (2019b) for details about the frame structure.

3 Measurement results and modeling

3.1 Two-path model

In this section, the channel measurement results and analysis are given. Our measurements were conducted in Tianfu Avenue, which is an eight-lane wide avenue that lies on the outskirts of Chengdu, China. We considered a 1900 m straight section in Tianfu Avenue for our long-distance channel measurements. A V2I communication measurement scenario was considered, as shown in Fig. 3, where the RX antenna was installed at the roadside and the TX antenna was fixed to the top of the vehicle. The height of the TX-RX antennas above the ground was configured to 2 m. During the measurement, the vehicle was driven toward the RX antenna at a constant speed of 50 km/h, and there were no moving vehicles/scatterers. According to our past work (Yu et al., 2019), the two horn antennas were always aligned to each other over 200 m. In the process of driving, we recorded the vehicle positions continuously. The vehicle went straight ahead, and there was no obvious shelter; thus, the TX and RX were always in line-of-sight (LoS) conditions.

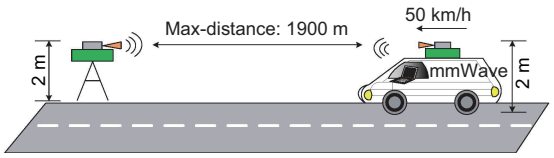

Fig. 3 A vehicle-to-infrastructure 1900-m communication measurement scenario

In fact, the multiple paths caused by all sorts of scatterers in Tianfu Avenue have significant impacts on the channel. The measurement scenario can be simplified as shown in Fig. 4. The distance between the TX and RX is denoted by r, which can be measured by the Global Positioning System (GPS) based distance measuring instrument.

There are two rays from the TX to the RX, including the direct path and the reflection path. For each path, the power of the signal is inversely proportional to the square of the communication distance. For the angular information, we have found in the past work that the azimuth angle that has the greatest RX power is 0° (Yu et al., 2019). If both the TX and RX antennas are kept in parallel to the road, the maximum antenna gain can be achieved for most of the time. In this study, we consider only the alignment of two antennas. We assume that the signal transmission angle is θ_1 and that the angle at which the signal reaches the RX is θ_2. Since the antenna gains of TX $g_1(\cdot)$ and RX $g_2(\cdot)$ vary in different directions, the changes of θ_1 and θ_2 during driving will lead to a change of gain, thus affecting the power of the received signal. Then, the beam patterns of TX and RX antennas can be represented by $g_1(\theta_1)$ and $g_2(\theta_2)$, respectively.

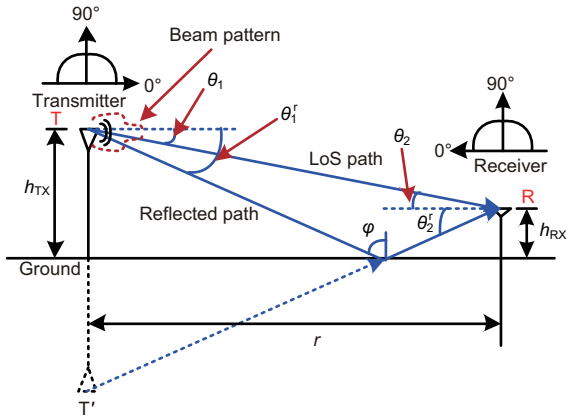

Fig. 4 Two-path model (LoS: line-of-sight)

The reflected path can be viewed as the LoS path emitted from the mirror image of TX (denoted by T′) relative to the ground, as indicated in Fig. 4. Therefore, the length of the reflected path is $d = \overline{\mathrm{T'R}}$, and the distance of the LoS path is $d = \overline{\mathrm{TR}}$. When the signal is reflected from the ground, it is necessary to consider the reflection coefficient $R(\varphi)$, where φ represents the angle of incidence. Generally, when an electromagnetic wave propagates from medium 1 to medium 2, the reflection of the electromagnetic wave on the surface of the medium can be classified into transverse electric (TE) polarization and transverse magnetic (TM) polarization according to whether the electric field or magnetic field is parallel to the incident surface (ITU, 2015).

When medium 1 is air, the reflection coefficients of TE polarization and TM polarization can be expressed as follows (ITU, 2012):

$$R_{\mathrm{TE}}=\frac{\cos\varphi-\sqrt{\eta-\sin^2\varphi}}{\cos\varphi+\sqrt{\eta-\sin^2\varphi}}, \tag{7}$$

$$R_{\mathrm{TM}}=\frac{\eta\cos\varphi-\sqrt{\eta-\sin^2\varphi}}{\eta\cos\varphi+\sqrt{\eta-\sin^2\varphi}}, \tag{8}$$

where η is the relative permittivity of medium 2.

Assuming that signal $s(t)=1$ is transmitted, the reflected signal received by the RX at a TX-RX distance r can be written as follows:

$$x_{\mathrm{re}}(r)=\frac{1}{\mathrm{T'R}}\mathrm{e}^{\mathrm{j}\frac{2\pi f_c\overline{\mathrm{T'R}}}{c}}R(\varphi)\sqrt{g_1(\theta_1^{\mathrm{r}})g_2(\theta_2^{\mathrm{r}})}, \tag{9}$$

where $\mathrm{e}^{\mathrm{j}\frac{2\pi f_c\overline{\mathrm{T'R}}}{c}}$ is the phase shift along the path, and θ_1^{r} and θ_2^{r} are the transmitted angle and received angle of reflection, respectively, as shown in Fig. 4.

The final received signal is the sum of the straight path signal and the reflection path signal (Parsons, 2000):

$$\begin{cases} x(r)=x_{\mathrm{LoS}}(r)+x_{\mathrm{re}}(r), \\ x_{\mathrm{LoS}}(r)=\frac{1}{\mathrm{TR}}\mathrm{e}^{\mathrm{j}\frac{2\pi f_c\overline{\mathrm{TR}}}{c}}\sqrt{g_1(\theta_1^{\mathrm{r}})g_2(\theta_2^{\mathrm{r}})}, \\ x_{\mathrm{re}}(r)=\frac{1}{\mathrm{T'R}}\mathrm{e}^{\mathrm{j}\frac{2\pi f_c\overline{\mathrm{T'R}}}{c}}R(\varphi)\sqrt{g_1(\theta_1^{\mathrm{r}})g_2(\theta_2^{\mathrm{r}})}. \end{cases} \tag{10}$$

3.2 Roughness parameters

In this two-path model, the ideal specular reflection is considered. However, the signal after specular reflection seriously affects the RSSI, which is at variance with reality. For a medium with a rough surface, part of the electromagnetic energy is lost due to the scattering by the rough surface.

To obtain better results, the widely adopted strategy in most recent studies to handle reflections from rough surfaces is to multiply the reflection coefficient by a scattering coefficient (ITU, 2012):

$$R_{\mathrm{rough}}=\rho_{\mathrm{s}}R_{\mathrm{smooth}}, \tag{11}$$

where the scattering coefficient ρ_{s} can be expressed as follows:

$$\rho_{\mathrm{s}}=\max\{\mathrm{e}^{-\frac{1}{2}g^2},\ 0.15\}, \tag{12}$$

where

$$g=\frac{4\pi\sigma}{\lambda}\cos\varphi. \tag{13}$$

Here, σ (cm) is the standard deviation of surface roughness and φ is the angle of incidence. The cut-off value of 0.15 in Eq. (12) is to prevent ρ_{s} from becoming too small. As σ gets close to zero, ρ_{s} approaches one and the rough surface degrades into the specular surface. Moreover, when TX and RX are very close to each other, the angle of incidence φ becomes close to 90° and the value of ρ_{s} approaches one.

Since the value of σ of the actual road is not given in existing research works, it is necessary to find the appropriate value of σ to satisfy the considered model. This rough reflector model is derived based on the assumption of small roughness. The value of σ must be smaller than the wavelength of 41 GHz mmWave (Zhou, 2017), which is approximately 7.32 mm.

We use mean squared error (MSE) criterion as the predictive evaluation indicator to obtain the best value of σ, so that we can make the RSSI of the rough surface model most consistent with the actual measurement data. The MSE criterion can be written as

$$\mathrm{MSE}=\frac{1}{M}\sum_{i=1}^{M}(\hat{y}_i-y_i)^2, \tag{14}$$

where $\hat{y}=\{\hat{y}_1,\hat{y}_2,\cdots,\hat{y}_n\}$ and $y=\{y_1,y_2,\cdots,y_n\}$ are the predicted and true RSSI values, respectively.

The result of MSE analysis is shown in Fig. 5, where the smallest MSE is 16.3506 dB when the corresponding best σ value is 0.119.

The comparison of the results of the two models and the measurement data is shown in Fig. 6: the model result with specular reflection is in red dotted line, the model result with the rough reflective surface is in green starred line, and the actual measurement data is in blue solid line. It can be seen that by considering road roughness, the deep fading of RSSI is significantly reduced compared to the case of the specular reflective surface. The RSSI result with the introduction of the scattering factor is more consistent with the raw data.

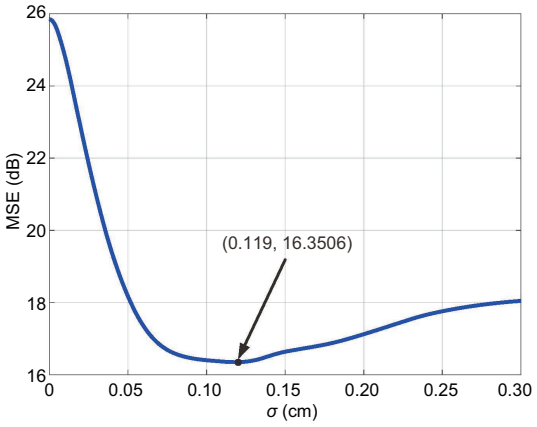

Fig. 5 Change in the mean squared error (MSE) as the surface roughness increases

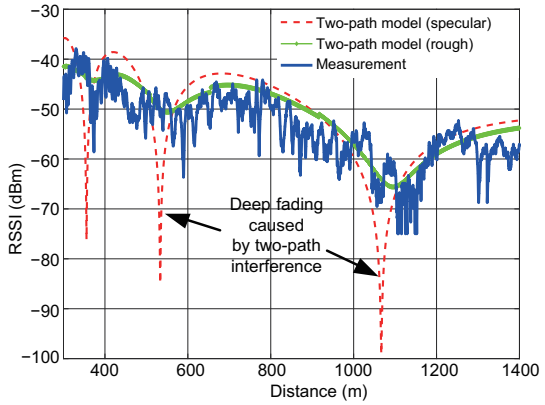

Fig. 6 Comparison of RSSI simulation results, including the specular and rough surface scenarios and the actual tests when the TX moves from 1900 m to the RX

RSSI: received signal strength indicator; RX: receiver; TX: transmitter. References to color refer to the online version of this figure

4 Path-loss model

4.1 CI-TRH model

The existing path-loss models include the CIF model (or the CI free space reference distance with a frequency-weighted path-loss exponent (PLE)) (MacCartney et al., 2015; Sun et al., 2016), the CI free space reference distance with a height-dependent PLE (CIH) model considering the influence of the height of a BS on the path loss in a rural environment (MacCartney and Rappaport, 2017), and the CI breakpoint (CI-BP) model adding the breakpoint distance (Yu et al., 2019).

These above models are almost derived from the CI free space reference distance path-loss model, referred to as the CI model. This is a classic model and is suitable for outdoor communication scenarios, expressed as follows (Rappaport et al., 2015):

$$\begin{aligned}\mathrm{PL}^{\mathrm{CI}}(f_{\mathrm{c}},d)\,(\mathrm{dB})=&\,\mathrm{FSPL}(f_{\mathrm{c}},d_0)\,(\mathrm{dB})+10n\lg\frac{d}{d_0}\\&+\chi_{\sigma}^{\mathrm{CI}},\quad d\geq d_0,\ d_0=1\ \mathrm{m},\end{aligned}\tag{15}$$

where FSPL denotes the free space path loss, d_0 denotes the free space reference distance (usually defined as 1 m), n denotes the PLE, and $\chi_{\sigma}^{\mathrm{CI}}$ denotes the shadow fading whose distribution is Gaussian distribution with zero mean and standard deviation σ in decibels. As can be seen, the CI model is controlled by two parameters: the 3D distance between TX and RX d (m) and the mmWave frequency f_{c} (GHz).

However, the CI model (as well as most existing models, such as the CIF model and the CI-BP model mentioned earlier) does not consider the TX-RX antenna heights as the modeling parameters. The TX-RX antenna heights have significant impacts on the large-scale path loss, as mentioned by MacCartney and Rappaport (2017).

The CIH model proposed by MacCartney and Rappaport (2017) considers only the TX height but ignores the impacts of the RX height. In practice, the TX and RX are only a few meters high in a V2I scenario; both of them are crucial, and their impacts on the path loss should be modeled. To solve this problem, we propose a new path-loss model derived from the CI model and the two-path model in Section 3, and apply it to the actual measurement scenario on the road. This model considers the influence of the heights of both TX and RX and hence is called the CI-TRH model. The CI-TRH model is represented as follows:

$$\begin{aligned}&\mathrm{PL}^{\text{CI-TRH}}(f,d,h_{\mathrm{TX}},h_{\mathrm{RX}})\,(\mathrm{dB})\\=&\,\mathrm{FSPL}(f_{\mathrm{c}},1\ \mathrm{m})\,(\mathrm{dB})+10n\lg d\\&\cdot\left(1+b_{\mathrm{TX}}\frac{h_{\mathrm{TX}}-h_{\mathrm{B}_0}}{h_{\mathrm{B}_0}}+b_{\mathrm{RX}}\frac{h_{\mathrm{RX}}-h_{\mathrm{B}_0}}{h_{\mathrm{B}_0}}\right)\\&+\chi_{\sigma}^{\text{CI-TRH}},\quad d\geq 1\ \mathrm{m},\end{aligned}\tag{16}$$

where h_{TX} and h_{RX} are the heights of the TX and RX, respectively, h_{B_0} is the average height of the TX and RX vehicles in the measurement, and n represents the distance dependence of CI-TRH path loss, the same as PLE in the CI model. We consider the influence of the heights of both TX and RX on PLE, so that we can observe the relationship between the height and PLE more intuitively compared with the traditional model.

b_{TX} and b_{RX} are related to the heights of TX and RX, respectively, and can evaluate the linear relationship between PLE and heights of TX and RX. Here, we define the CI-TRH PLE that is equivalent to the PLE in the CI model as

$$\mathrm{PLE}_{\mathrm{equ}}=n\left(1+b_{\mathrm{TX}}\frac{h_{\mathrm{TX}}-h_{\mathrm{B}_0}}{h_{\mathrm{B}_0}}+b_{\mathrm{RX}}\frac{h_{\mathrm{RX}}-h_{\mathrm{B}_0}}{h_{\mathrm{B}_0}}\right).\tag{17}$$

The specific parameters of the CI-TRH model are shown in Table 2. Thus, in the CI-TRH model, only three parameters, namely, n, b_{TX}, and b_{RX}, need to be considered and optimized. The detailed derivation process of the closed-form solutions of

these three optimization parameters is shown in the Appendix.

In our experiment, we obtain the results only when TX and RX heights are both 2 m; however, it is necessary to consider the relationship between different TX heights, RX heights, and PLEs. The relationship among the TX height (1–6 m), the RX height (1–4 m, the RX height is usually smaller than the TX height), and PLE is depicted in Fig. 7. It can be seen that when the TX height increases from 1 to 6 m, PLE increases by 0.039, with an average increase of 0.0078/m. When the RX height increases from 1 to 4 m, PLE increases by 0.0257, with an average increase of 0.0086/m.

Fig. 8 shows the simulation results of the CI and CI-TRH models, comparing them to the actual data. The result under the first 100 m is seriously affected by the beam misalignment, and hence is not considered. PLEs of the CI-TRH and CI models are 2.0725 and 2.065, respectively. These results are close to the value of PLE (=2) in the free space path loss.

Moreover, the value of shadow fading in the CI model is 4.69, while it is 4.68 in the CI-TRH model, revealing that the proposed CI-TRH model has almost the same performance as the classic CI model. The proposed CI-TRH provides better insights into how the heights of TX and RX antennas affect the large-scale path loss.

4.2 RMS delay spread

The influence of multipath channels on wireless signals is manifested as multipath fading characteristics, and usually, a wireless multipath channel can be regarded as a filter acting on the channel. CIR in a broadband transmission system can be expressed as follows:

$$h(t,\tau)=\sum_i a_i \mathrm{e}^{-\mathrm{j}\psi_i(t)}\mathrm{ffi}(t-\tau_i), \tag{18}$$

where a_i and τ_i represent the actual amplitude and the incremental delay of the i^{th} component, respectively, the phase $\psi_i(t)$ results from the accumulation of all multipath components (MPCs) in the i^{th} excess delay, and $\mathrm{ffi}(\cdot)$ is the unit impulse function.

The time dispersion characteristics of a multipath channel can be described by the RMS delay spread σ_τ. In fact, the RMS delay spread is the normalized second-order central moment of the PDP.

Table 2 CI-TRH model parameters

Parameter	Value
f_c (GHz)	41
h_{B_0} (m)	2
TX height range (m)	1–6
RX height range (m)	1–4
n	0.9947
b_{TX}	0.0157
b_{RX}	0.0172
$\chi_\sigma^{\text{CI-TRH}}$ (dB)	4.726
PLE	2.0054

CI-TRH: close-in model considering TX and RX heights; f_c: mmWave frequency; h_{B0}: average height of TX and RX vehicles; PLE: path-loss exponent; RX: receiver; TX: transmitter

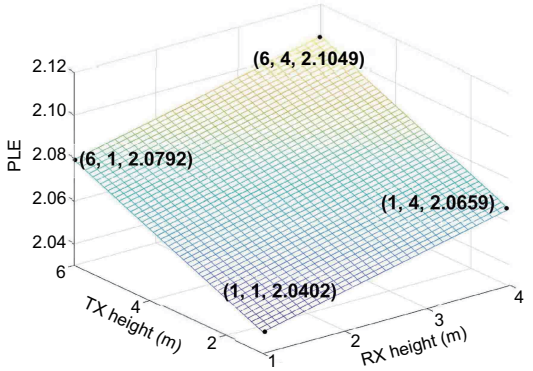

Fig. 7 Three-dimensional relationship between PLE and the heights of TX and RX

PLE: path-loss exponent; RX: receiver; TX: transmitter

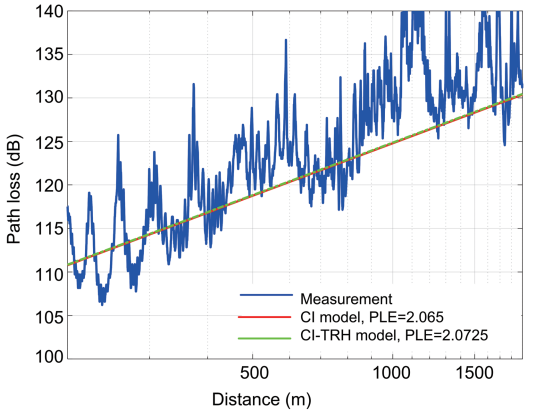

Fig. 8 Comparison of the path loss of the measurement, CI model, and CI-TRH model

CI: close-in; CI-TRH: CI model considering the heights of TX and TX; PLE: path-loss exponent; RX: receiver; TX: transmitter. References to color refer to the online version of this figure

According to the above expression of average additional delay, the RMS delay spread σ_τ can be denoted as follows:

$$\sigma_\tau=\sqrt{E(\tau^2)-\bar{\tau}^2}, \tag{19}$$

where $E(\tau^2)=\sum_k a_k^2\tau_2^2/\sum_k a_k^2$, and $\bar{\tau}$ denotes the

average excess delay, which can be written as

$$\bar{\tau}=\sum_k a_k^2\tau_k/\sum_k a_k^2. \tag{20}$$

Since the RMS delay spread is always nonnegative, it is modeled as a log-normal random variable in most existing studies (Yue et al., 2019b; Yan et al., 2020). Fig. 9 depicts the cumulative distribution function (CDF) of the measured RMS delay spread and its comparison with the standard log-normal distribution. The measured RMS delay ranges from 2 to 35 ns and its mean is 6.99 ns.

By fitting the RMS delay spread values, it can be discovered that the measured RMS delay data matches well with the log-normal prediction $N_{\log}(1.78,\ 0.58^2)$. By comparing this result with those of other studies, such as indoor measurements (Yue et al., 2019a), the RMS delay spread value in this study is relatively large. The reason can be attributed to the fact that our measurement environment is much more complex than indoor environments, which includes roadside facilities, bushes, and passing vehicles, which serve as scatterers, causing a large number of MPCs.

Apart from analyzing the overall distribution of RMS delay spread, it is necessary to discuss the relationship between the RMS delay spread on one hand and the distance between TX and RX on the other hand. An efficient way to study the dependence of RMS delay is to partition the raw data obtained along the TX-RX track into a number of bins, so that the CIRs in each bin can be regarded as stationary.

In our study, a total number of 120 bins are considered in our partition because when the number of sections reaches 120, the slope k and intercept b of the fitted line converge to a stable value, as illustrated in Fig. 10, and the stable values for the slope and intercept are −0.004 048 (from Fig. 10, the slope is negative) and 10.97, respectively. As depicted in Fig. 11, we use the widely adopted linear fitting (solid red line) to process the average RMS delay spread obtained in each bin (blue dots) at different locations along the TX-RX track. With an increase in the distance, the value of RMS delay spread decreases. This result is corresponding to that of other researches, such as Matolak and Sun (2014). In fact, the reason why RMS delay decreases with the increase in the TX-RX distance is that the numerous scatterers are filtered by the narrow-beam antenna, so the LoS path fades much slower than the scattered paths.

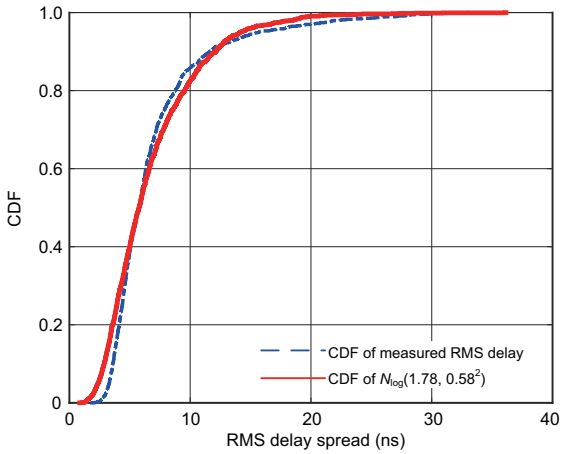

Fig. 9 CDF of the actually measured RMS delay spread and the fitted log-normal distribution
CDF: cumulative distribution function; RMS: root-mean-square

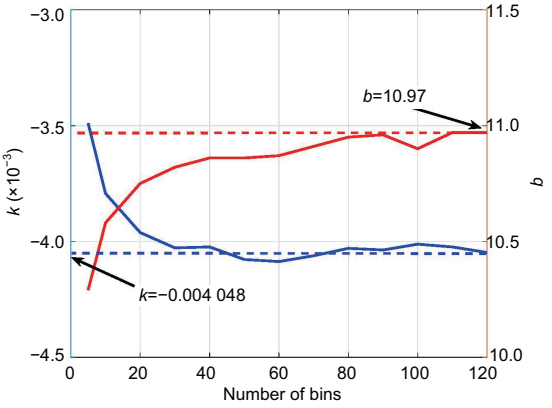

Fig. 10 Convergence trend of the slope k and intercept b with different number of bins

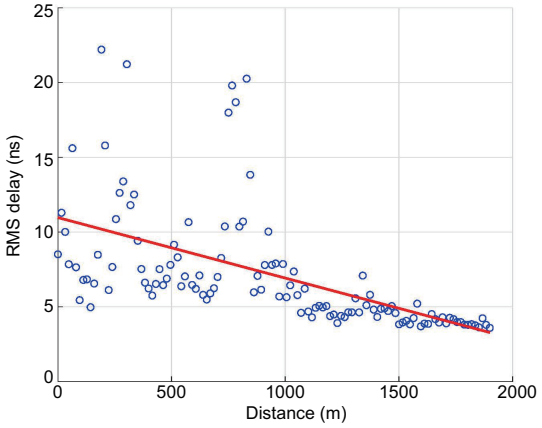

Fig. 11 RMS delay distribution versus distance
RMS: root-mean-square. References to color refer to the online version of this figure

4.3 PDP modeling

In urban environments, PDP is often modeled with the exponential fading model, as follows:

$$P(\tau)=|h(t,\tau)|^2=a\mathrm{e}^{-b\tau}. \tag{21}$$

On the basis of Eq. (21), a more general PDP model, named the two-section exponential model, has been proposed by Yue et al. (2019b), which divides the PDP curve into two sections. The motivation of using this model is that the two-section exponential model is more common. The one-section exponential model is easily effected by the noise floor. The two-section exponential model covers all applicable cases of the one-section exponential model and can solve the problem of noise floor:

$$P(\tau)=\begin{cases}0, & \tau<0,\\ 1, & \tau=0,\\ a_1\mathrm{e}^{-b_1\tau}, & 0<\tau<\tau_\mathrm{c},\\ P(\tau_\mathrm{c})\mathrm{e}^{-b_2(\tau-\tau_\mathrm{c})}, & \tau\geq\tau_\mathrm{c},\end{cases} \tag{22}$$

where a_1, b_1, b_2, and τ_c are the PDP shape parameters whose values are determined by the measurement data (Yue et al., 2019b).

The problem with the PDP model of Yue et al. (2019b) is the difficulty in determining τ_c, because a change in τ_c will lead to a different value of b_2. In other words, there will be an error propagation problem; i.e., the errors in determining τ_c will lead to errors in determining b_2. To address this problem, we modify the PDP model of Yue et al. (2019b) into a more general form, which can be written as follows:

$$P(\tau)=\begin{cases}0, & \tau<0,\\ 1, & \tau=0,\\ a_1\mathrm{e}^{-b_1\tau}, & 0<\tau<\tau_\mathrm{c},\\ a_2\mathrm{e}^{-b_2\tau}, & \tau\geq\tau_\mathrm{c},\end{cases} \tag{23}$$

where a_1, b_1, a_2, b_2, and τ_c are the PDP shape parameters whose values are to be studied. The difference between the modified model in Eq. (23) and the PDP model of Yue et al. (2019b) is that the dependence of the second section on τ_c is relieved. In the modified model, a_1, b_1, a_2, and b_2 are determined independently at first, and then τ_c is determined according to the intersections of the two sections. Fig. 12 gives the real PDP and its model fitting.

It can be seen that this modified model result matches well with the raw data. Moreover, the measured PDP over the distance is shown in Fig. 13, showing the trend of V2I channel variations. The captured PDP snapshots are aligned according to their strongest path at the reference delay of $\tau=0$ ns. Some small "bumps" are present in the PDP versus distance plot; this is caused by the vibration of the vehicle during driving. With the increase in the distance, the multipath effect is gradually weakened, which proves that the value of RMS delay spread decreases with the increase in the distance.

Note that we have proposed a two-path model with a roughness factor to model the path loss for the V2I scenario. Here, we propose the use of another model, namely, the two-section exponential PDP model, to model the special characteristics of the MPCs.

Fig. 14 shows the CDFs of the PDP shape

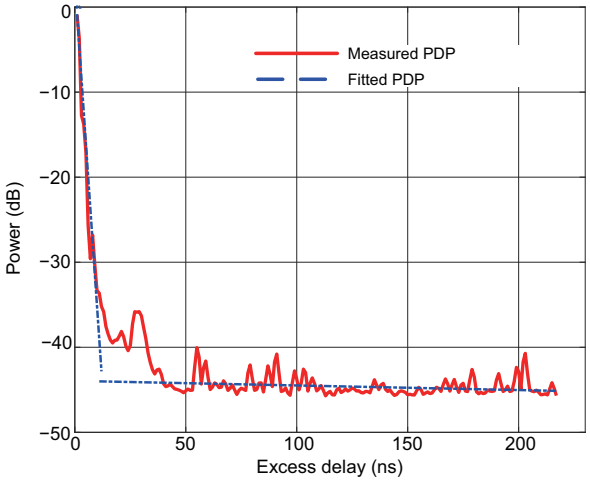

Fig. 12 Measured power delay profile (PDP) and the corresponding best fit with the improved two-section exponential model

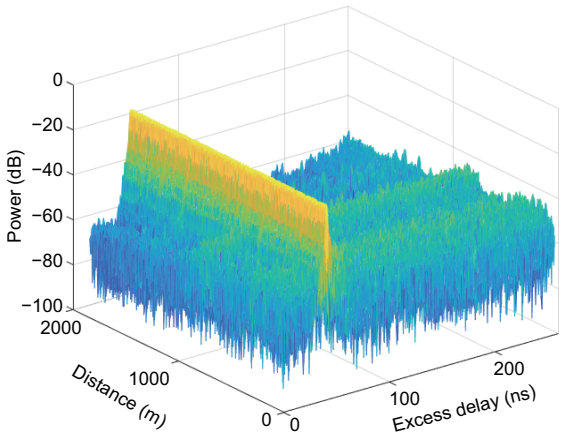

Fig. 13 Measured power delay profile over the distance

parameters a_1, b_1, a_2, b_2, and τ_c obtained from our measurement data and compares them with the corresponding normal or log-normal distributions. The results show that a_1 and a_2 can be modeled by log-normal distributions, $N_{\log}(-3.05, 1.43^2)$ and $N_{\log}(-11.33, 1.17^2)$, respectively, while b_1, b_2, and τ_c have normal distributions, $N(0.35, 0.21^2)$, $N(0.001\ 03, 0.0015^2)$, and $N(25.91, 7.16^2)$, respectively.

Fig. 15 depicts the relationship between the shape parameters (blue dots) and the TX-RX distance, using the linear fitting (solid red line) to describe their general trend versus the distance. The results show that both a_1 and b_1 increase with the increase in the distance, a_2 decreases with the distance, b_2 and τ_c are basically constant around a fixed value, and a_2 is the most sensitive to the change in the TX-RX distance.

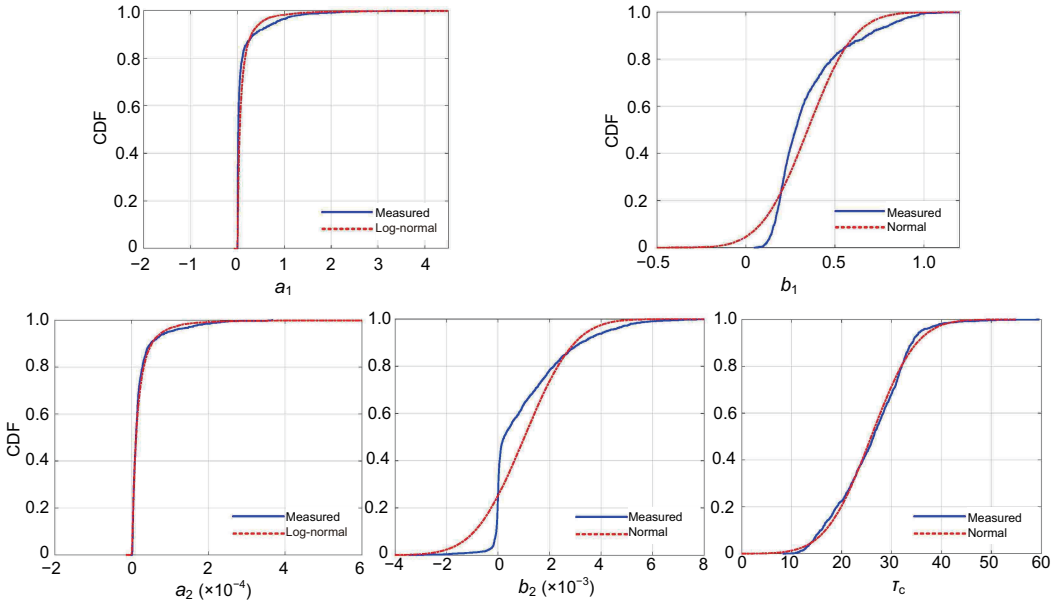

Fig. 14 Cumulative distribution functions (CDFs) of the actual measured shape parameters a_1, b_1, a_2, b_2, and τ_c and their corresponding best matching distributions of $N_{\log}(-3.05, 1.43^2)$, $N(0.35, 0.21^2)$, $N_{\log}(-11.33, 1.17^2)$, $N(0.001\ 03, 0.0015^2)$, and $N(25.91, 7.16^2)$

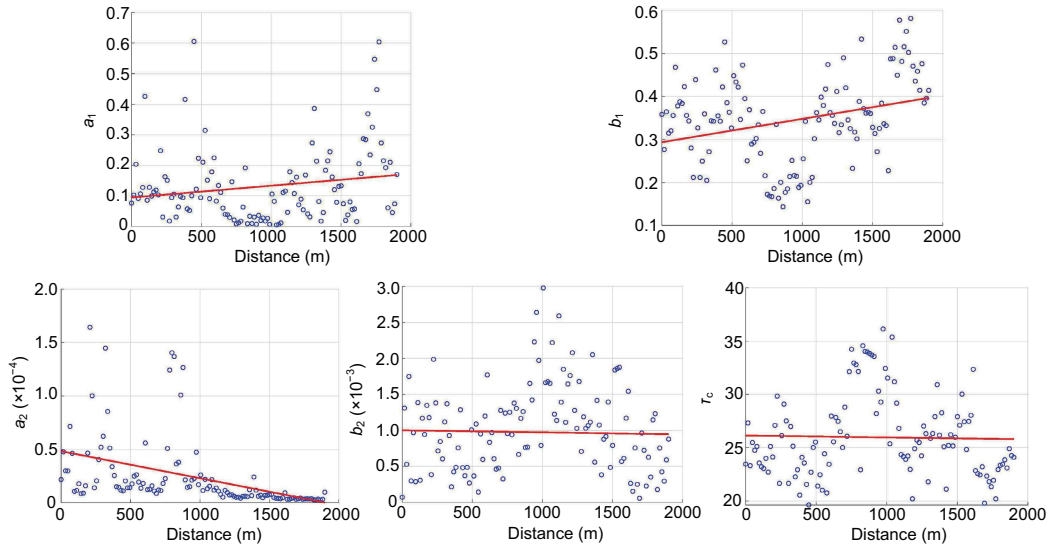

Fig. 15 Relationship between the actual measured shape parameters a_1, b_1, a_2, b_2, τ_c and the distance (References to color refer to the online version of this figure)

5 Conclusions

We have introduced our long-distance V2I mmWave measurement study at the frequency of 41 GHz. Based on the verified two-path model, a novel path-loss model has been developed to better characterize the impacts of antenna heights on the large-scale path loss. Moreover, the channel characteristic parameters such as RSSI, RMS delay spread, and PDP have been modeled. Our study showed that a larger discrepancy in the TX and RX antenna heights results in a larger PLE, and that the overall PLE ranges from 2.0402 to 2.1049 in V2I long-distance communication scenarios. We found that the RMS delay spread decreases as the distance increases, which is caused by the faster loss in the energy of the reflected and scattered paths, compared with the LoS path. Some PDP parameters, such as b_2 and τ_c, are insensitive to the distance, whereas some other parameters such as a_1, b_1, and a_2 change significantly with the distance. However, other factors, such as street lights, bushes, and RX directions, can affect highway mmWave channels inevitably. In our future research, we will consider richer channel characterization parameters and more complex communication environments, such as the effect of the moving vehicles/scatterers. To achieve the purpose of studying road mmWave channels comprehensively, more parameters describing channel characteristics, such as Doppler spread, will be analyzed.

Contributors

Lin YANG designed the research. Xichen LIU and Daizhong YU processed the data. Xichen LIU drafted the manuscript. Daizhong YU helped organize the manuscript. Xichen LIU, Lin YANG, and Daizhong YU revised and finalized the paper.

Compliance with ethics guidelines

Xichen LIU, Lin YANG, and Daizhong YU declare that they have no conflict of interest.

References

Analog Devices, 2013. AD8362: 50 Hz to 3.8 GHz 65 dB TruPwr^{TM} Detector. Norwood, MA 02062-9106, USA.

Bernadó L, Zemen T, Tufvesson F, et al., 2015. Time- and frequency-varying K-factor of non-stationary vehicular channels for safety-relevant scenarios. *IEEE Trans Intell Transp Syst*, 16(2):1007-1017. https://doi.org/10.1109/TITS.2014.2349364

Blumenstein J, Vychodil J, Pospisil M, et al., 2016. Effects of vehicle vibrations on mm-wave channel: Doppler spread and correlative channel sounding. Proc IEEE 27th Annual Int Symp on Personal, Indoor, and Mobile Radio Communications, p.1-5. https://doi.org/10.1109/PIMRC.2016.7794619

Blumenstein J, Prokes A, Vychodil J, et al., 2017. Time-varying K factor of the mm-Wave vehicular channel: velocity, vibrations and the road quality influence. Proc IEEE 28th Annual Int Symp on Personal, Indoor, and Mobile Radio Communications, p.1-5. https://doi.org/10.1109/PIMRC.2017.8292755

Blumenstein J, Prokes A, Vychodil J, et al., 2018. Measured high-resolution power-delay profiles of nonstationary vehicular millimeter wave channels. Proc IEEE 29th Annual Int Symp on Personal, Indoor and Mobile Radio Communications, p.1-5. https://doi.org/10.1109/PIMRC.2018.8580949

Boban M, Dupleich D, Iqbal N, et al., 2019. Multi-band vehicle-to-vehicle channel characterization in the presence of vehicle blockage. *IEEE Access*, 7:9724-9735. https://doi.org/10.1109/ACCESS.2019.2892238

Groll H, Zöchmann E, Pratschner S, et al., 2019. Sparsity in the delay-Doppler domain for measured 60 GHz vehicle-to-infrastructure communication channels. Proc IEEE Int Conf on Communications Workshops, p.1-6. https://doi.org/10.1109/ICCW.2019.8756930

Guan K, He DP, Ai B, et al., 2018. Realistic channel characterization for 5G millimeter-wave railway communications. Proc IEEE Globecom Workshops, p.1-6. https://doi.org/10.1109/GLOCOMW.2018.8644076

He DP, Ai B, Guan K, et al., 2018. Channel measurement, simulation, and analysis for high-speed railway communications in 5G millimeter-wave band. *IEEE Trans Intell Transp Syst*, 19(10):3144-3158. https://doi.org/10.1109/TITS.2017.2771559

He DP, Wang LH, Guan K, et al., 2019. Channel characterization for mmWave vehicle-to-infrastructure communications in urban street environment. Proc 13th European Conf on Antennas and Propagation, p.1-5.

IEEE, 2012. Wireless LAN Medium Access Control (MAC) and Physical Layer (PHY) Specifications Amendment 3: Enhancements for very High Throughput in the 60 GHz Band. IEEE Standard 802.11ad-2012.

ITU, 2012. Propagation Data and Prediction Methods Required for the Design of Terrestrial Broadband Radio Access Systems Operating in a Frequency Range from 3 to 60 GHz. ITU-R P.1410-5.

ITU, 2015. Effects of Building Materials and Structures on Radiowave Propagation above about 100 MHz. ITU-R P.2040-1.

Lei MY, Zhang JH, Lei T, et al., 2016. 28-GHz indoor channel measurements and analysis of propagation characteristics. Proc IEEE 25th Annual Int Symp on Personal, Indoor, and Mobile Radio Communication, p.208-212. https://doi.org/10.1109/PIMRC.2014.7136161

MacCartney GRJr, Rappaport TS, 2017. Rural macrocell path loss models for millimeter wave wireless communications. *IEEE J Sel Areas Commun*, 35(7):1663-1677. https://doi.org/10.1109/JSAC.2017.2699359

MacCartney GRJr, Rappaport TS, Sun S, et al., 2015. Indoor office wideband millimeter-wave propagation measurements and channel models at 28 and 73 GHz for ultra-dense 5G wireless networks. *IEEE Access*, 3:2388-2424. https://doi.org/10.1109/ACCESS.2015.2486778

Matolak DW, Sun RY, 2014. Initial results for air-ground channel measurements & modeling for unmanned aircraft systems: over-sea. Proc IEEE Aerospace Conf, p.1-15. https://doi.org/10.1109/AERO.2014.6836369

Mecklenbrauker CF, Molisch AF, Karedal J, et al., 2011. Vehicular channel characterization and its implications for wireless system design and performance. *Proc IEEE*, 99(7):1189-1212. https://doi.org/10.1109/JPROC.2010.2101990

Meinel H, Plattner A, 1983. Millimetre-wave propagation along railway lines. *IEE Proc F Commun Radar Signal Process*, 130(7):688-694. https://doi.org/10.1049/ip-f-1.1983.0102

Park JJ, Lee J, Kim KW, et al., 2018. 28 GHz Doppler measurements in high-speed expressway environments. Proc IEEE 29th Annual Int Symp on Personal, Indoor and Mobile Radio Communications, p.1132-1133. https://doi.org/10.1109/PIMRC.2018.8580954

Parsons, 2000. The Mobile Radio Propagation Channel (2nd Ed.). John Wiley & Sons, New York, USA.

Popović BM, 1999. Efficient golay correlator. *Electron Lett*, 35(17):1427-1428. https://doi.org/10.1049/el:19991019

Prokes A, Vychodil J, Pospisil M, et al., 2016. Time-domain nonstationary intra-car channel measurement in 60 GHz band. Proc Int Conf on Advanced Technologies for Communications, p.1-6. https://doi.org/10.1109/ATC.2016.7764753

Prokes A, Vychodil J, Mikulasek T, et al., 2018. Time-domain broadband 60 GHz channel sounder for vehicle-to-vehicle channel measurement. Proc IEEE Vehicular Networking Conf, p.1-7. https://doi.org/10.1109/VNC.2018.8628344

Rahman AU, Chandra A, Prokes A, et al., 2019. Doppler characteristics of 60 GHz mmWave I2I channels. Proc ICC IEEE Int Conf on Communications, p.1-6. https://doi.org/10.1109/ICC.2019.8761798

Rappaport TS, MacCartney GR, Samimi MK, et al., 2015. Wideband millimeter-wave propagation measurements and channel models for future wireless communication system design. *IEEE Trans Commun*, 63(9):3029-3056. https://doi.org/10.1109/TCOMM.2015.2434384

Sánchez MG, Táboas MP, Cid EL, 2017. Millimeter wave radio channel characterization for 5G vehicle-to-vehicle communications. *Measurement*, 95:223-229. https://doi.org/10.1016/j.measurement.2016.10.018

Soliman M, Dawoud Y, Sand S, et al., 2018. Influences of train wagon vibrations on the mmwave wagon-to-wagon channel. Proc 12th European Conf on Antennas and Propagation, p.1-5. https://doi.org/10.1049/cp.2018.0962

Sun S, Rappaport TS, Thomas TA, et al., 2016. Investigation of prediction accuracy, sensitivity, and parameter stability of large-scale propagation path loss models for 5G wireless communications. *IEEE Trans Veh Technol*, 65(5):2843-2860. https://doi.org/10.1109/TVT.2016.2543139

Yan D, Guan K, He DP, et al., 2020. Channel characterization for vehicle-to-infrastructure communications in millimeter-wave band. *IEEE Access*, 8:42325-42341. https://doi.org/10.1109/ACCESS.2020.2977208

Yang BQ, Yu ZQ, Zhang RQ, et al., 2019. Local oscillator phase shifting and harmonic mixing-based high-precision phased array for 5G millimeter-wave communications. *IEEE Trans Microw Theory Tech*, 67(7):3162-3173. https://doi.org/10.1109/TMTT.2019.2899598

Yu DZ, Yue GR, Wei N, et al., 2019. Empirical study on directional millimeter-wave propagation in railway communications between train and trackside. *IEEE J Sel Areas Commun*, 38(12):2931-2945. https://doi.org/10.1109/JSAC.2020.3005488

Yue GR, Yu DZ, Qiu H, et al., 2019a. Measurements and ray tracing simulations for non-line-of-sight millimeter-wave channels in a confined corridor environment. *IEEE Access*, 7:85066-85081. https://doi.org/10.1109/ACCESS.2019.2924510

Yue GR, Yu DZ, Cheng L, et al., 2019b. Millimeter-wave system for high-speed train communications between train and trackside: system design and channel measurements. *IEEE Trans Veh Technol*, 68(12):11746-11761. https://doi.org/10.1109/TVT.2019.2919625

Zhang X, Qiu G, Zhang JH, et al., 2019. Analysis of millimeter-wave channel characteristics based on channel measurements in indoor environments at 39 GHz. Proc 11th Int Conf on Wireless Communications and Signal Processing, p.1-6. https://doi.org/10.1109/WCSP.2019.8928017

Zhou CM, 2017. Ray tracing and modal methods for modeling radio propagation in tunnels with rough walls. *IEEE Trans Antenn Propag*, 65(5):2624-2634. https://doi.org/10.1109/TAP.2017.2677398

Zöchmann E, Mecklenbrauker CF, Lerch M, et al., 2018. Measured delay and Doppler profiles of overtaking vehicles at 60 GHz. Proc 12th European Conf on Antennas and Propagation, p.1-5. https://doi.org/10.1049/cp.2018.0470

Zöchmann E, Hofer M, Lerch M, et al., 2019. Position-specific statistics of 60 GHz vehicular channels during overtaking. *IEEE Access*, 7:14216-14232. https://doi.org/10.1109/ACCESS.2019.2893136

Appendix: Derivation of the CI-TRH model

To obtain the closed-form solutions of n, b_{TX}, and b_{RX}, we use the method that minimizes the minimum MSE, or equivalently, $\chi_\sigma^{\text{CI-TRH}}$.

The expression of the CI-TRH path-loss model can be written in the following form:

$$\begin{aligned}&\mathrm{PL}^{\text{CI-TRH}}(f,d,h_{\mathrm{TX}},h_{\mathrm{RX}})\,(\mathrm{dB})\\=&\mathrm{FSPL}(f_{\mathrm{c}},1\ \mathrm{m})\,(\mathrm{dB})+10\lg d\\&\cdot\left[n(2-b_{\mathrm{TX}}-b_{\mathrm{RX}})+\frac{nb_{\mathrm{TX}}}{h_{\mathrm{B}_0}}h_{\mathrm{TX}}+\frac{nb_{\mathrm{RX}}}{h_{\mathrm{B}_0}}h_{\mathrm{RX}}\right]\\&+\chi_\sigma^{\text{CI-TRH}},\quad d\geq 1\ \mathrm{m}.\end{aligned}\tag{A1}$$

Set $X=\mathrm{PL}^{\text{CI-HTR}}-\mathrm{FSPL}(f_{\mathrm{c}},1\ \mathrm{m})\,(\mathrm{dB})$ and $Y=10\lg d$, and let $\alpha=n(2-b_{\mathrm{RX}}-b_{\mathrm{TX}})$, $\beta_1=nb_{\mathrm{TX}}/h_{\mathrm{B}_0}$, $\beta_2=nb_{\mathrm{RX}}/h_{\mathrm{B}_0}$. The difference between the value of the CI-TRH model and the empirical data can be written as follows:

$$\chi_\sigma^{\text{CI-TRH}}=X-Y(a+\beta_1h_{\mathrm{TX}}+\beta_2h_{\mathrm{RX}}).\tag{A2}$$

Based on Eq. (A2), the standard deviation of $\chi_\sigma^{\text{CI-TRH}}$ can be expressed as follows:

$$\begin{aligned}\sigma^{\text{CI-TRH}}&=\sqrt{\tfrac{1}{N}\textstyle\sum\left(\chi_\sigma^{\text{CI-TRH}}\right)^2}\\&=\sqrt{\tfrac{1}{N}\textstyle\sum\left[X-Y(\alpha+\beta_1h_{\mathrm{TX}}+\beta_2h_{\mathrm{RX}})\right]^2},\end{aligned}\tag{A3}$$

where N is the number of all measured data. To obtain the minimum of $\sigma^{\text{CI-TRH}}$, we find the partial derivatives of $\sum\left[X-Y(\alpha+\beta_1h_{\mathrm{TX}}+\beta_2h_{\mathrm{RX}})\right]^2$ with respect to α, β_1, and β_2, and make them equal to zero:

$$\begin{aligned}&\frac{\partial}{\partial\alpha}\sum\left[X-Y(\alpha+\beta_1h_{\mathrm{TX}}+\beta_2h_{\mathrm{RX}})\right]^2\\&=\sum\left[-2Y(X-Y\alpha-\beta_1Yh_{\mathrm{TX}}-\beta_2Yh_{\mathrm{RX}})\right]\\&=\sum\left[2Y(\alpha Y+\beta_1Yh_{\mathrm{TX}}+\beta_2Yh_{\mathrm{RX}}-X)\right]\\&=2\Big(\alpha\textstyle\sum Y^2+\beta_1\sum Y^2h_{\mathrm{TX}}+\beta_2\sum Y^2h_{\mathrm{RX}}-\sum XY\Big)\\&=0,\end{aligned}\tag{A4}$$

$$\begin{aligned}&\frac{\partial}{\partial\beta_1}\sum\left[X-Y(\alpha+\beta_1h_{\mathrm{TX}}+\beta_2h_{\mathrm{RX}})\right]^2\\=&\sum\left[-2Yh_{\mathrm{TX}}(X-Ya-\beta_1Yh_{\mathrm{TX}}-\beta_2Yh_{\mathrm{RX}})\right]\\=&2\Big(\alpha\textstyle\sum Y^2h_{\mathrm{TX}}+\beta_1\sum Y^2h_{\mathrm{TX}}^2+\beta_2\sum Y^2h_{\mathrm{TX}}h_{\mathrm{RX}}\\&-\sum XYh_{\mathrm{TX}}\Big)\\=&0,\end{aligned}\tag{A5}$$

$$\begin{aligned}&\frac{\partial}{\partial\beta_2}\sum\left[X-Y(\alpha+\beta_1h_{\mathrm{TX}}+\beta_2h_{\mathrm{RX}})\right]^2\\=&\sum\left[-2Yh_{\mathrm{RX}}(X-Y\alpha-\beta_1Yh_{\mathrm{TX}}-\beta_2Yh_{\mathrm{RX}})\right]\\=&2\Big(\alpha\textstyle\sum Y^2h_{\mathrm{RX}}+\beta_1\sum Y^2h_{\mathrm{RX}}h_{\mathrm{TX}}+\beta_2\sum Y^2h_{\mathrm{RX}}^2\\&-\sum XYh_{\mathrm{RX}}\Big)\\=&0,\end{aligned}\tag{A6}$$

which can be simplified into the following forms:

$$\begin{aligned}&\alpha\textstyle\sum Y^2+\beta_1\sum Y^2h_{\mathrm{TX}}+\beta_2\sum Y^2h_{\mathrm{RX}}\\=&\textstyle\sum XY,\end{aligned}\tag{A7}$$

$$\begin{aligned}&\alpha\textstyle\sum Y^2h_{\mathrm{TX}}+\beta_1\sum Y^2h_{\mathrm{TX}}^2+\beta_2\sum Y^2h_{\mathrm{TX}}h_{\mathrm{RX}}\\=&\textstyle\sum XYh_{\mathrm{TX}},\end{aligned}\tag{A8}$$

$$\begin{aligned}&\alpha\textstyle\sum Y^2h_{\mathrm{RX}}+\beta_1\sum Y^2h_{\mathrm{RX}}h_{\mathrm{TX}}+\beta_2\sum Y^2h_{\mathrm{RX}}^2\\=&\textstyle\sum XYh_{\mathrm{RX}}.\end{aligned}\tag{A9}$$

Furthermore, writing Eqs. (A4)–(A6) in a matrix form yields

$$\begin{aligned}&\begin{pmatrix}\sum Y^2&\sum Y^2h_{\mathrm{TX}}&\sum Y^2h_{\mathrm{RX}}\\\sum Y^2h_{\mathrm{TX}}&\sum Y^2h_{\mathrm{TX}}^2&\sum Y^2h_{\mathrm{TX}}h_{\mathrm{RX}}\\\sum Y^2h_{\mathrm{RX}}&\sum Y^2h_{\mathrm{TX}}h_{\mathrm{RX}}&\sum Y^2h_{\mathrm{RX}}^2\end{pmatrix}\\&\cdot\begin{pmatrix}\alpha\\\beta_1\\\beta_2\end{pmatrix}=\begin{pmatrix}\sum XY\\\sum XYh_{\mathrm{TX}}\\\sum XYh_{\mathrm{RX}}\end{pmatrix}.\end{aligned}\tag{A10}$$

Finally, the closed-form solutions of α, β_1, and β_2 can be obtained:

$$\begin{aligned}&\begin{pmatrix}\alpha\\\beta_1\\\beta_2\end{pmatrix}=\\&\begin{pmatrix}\sum Y^2&\sum Y^2h_{\mathrm{TX}}&\sum Y^2h_{\mathrm{RX}}\\\sum Y^2h_{\mathrm{TX}}&\sum Y^2h_{\mathrm{TX}}^2&\sum Y^2h_{\mathrm{TX}}h_{\mathrm{RX}}\\\sum Y^2h_{\mathrm{RX}}&\sum Y^2h_{\mathrm{TX}}h_{\mathrm{RX}}&\sum Y^2h_{\mathrm{RX}}^2\end{pmatrix}^{-1}\\&\cdot\begin{pmatrix}\sum XY\\\sum XYh_{\mathrm{TX}}\\\sum XYh_{\mathrm{RX}}\end{pmatrix}.\end{aligned}\tag{A11}$$

After obtaining α, β_1, and β_2, we can use them to find the optimal values of n, b_{TX}, and b_{RX}:

$$n=\alpha+\beta_1h_{\mathrm{B}_0}+\beta_2h_{\mathrm{B}_0},\tag{A12}$$

$$b_{\mathrm{TX}}=\frac{2\beta_1h_{\mathrm{B}_0}}{\alpha+\beta_1h_{\mathrm{B}_0}+\beta_2h_{\mathrm{B}_0}},\tag{A13}$$

$$b_{\mathrm{RX}}=\frac{2\beta_2h_{\mathrm{B}_0}}{\alpha+\beta_1h_{\mathrm{B}_0}+\beta_2h_{\mathrm{B}_0}}.\tag{A14}$$